JACS
JOURNAL OF THE AMERICAN CHEMICAL SOCIETY
Article
pubs.acs.org/JACS

Tracking Catalyst Redox States and Reaction Dynamics in Ni–Fe Oxyhydroxide Oxygen Evolution Reaction Electrocatalysts: The Role of Catalyst Support and Electrolyte pH

Mikaela Görlin,[†,‡] Jorge Ferreira de Araújo,[†] Henrike Schmies,[†] Denis Bernsmeier,[†] Sören Dresp,[†] Manuel Gliech,[†] Zenonas Jusys,[§] Petko Chernev,[‡] Ralph Kraehnert,[†] Holger Dau,*[,‡] and Peter Strasser*[,†]

[†]Department of Chemistry, Chemical Engineering Division, Technical University of Berlin, Straße des 17. Juni 124, 10623, Berlin, Germany

[‡]Department of Physics, Free University of Berlin, Arnimallee 14, 14195, Berlin, Germany

[§]Institute of Surface Chemistry and Catalysis, Ulm University, Albert-Einstein-Allee 47, 89081, Ulm, Germany

Supporting Information

ABSTRACT: Ni–Fe oxyhydroxides are the most active known electrocatalysts for the oxygen evolution reaction (OER) in alkaline electrolytes and are therefore of great scientific and technological importance in the context of electrochemical energy conversion. Here we uncover, investigate, and discuss previously unaddressed effects of conductive supports and the electrolyte pH on the Ni–Fe(OOH) catalyst redox behavior and catalytic OER activity, combining *in situ* UV–vis spectro-electrochemistry, *operando* electrochemical mass spectrometry (DEMS), and *in situ* cryo X-ray absorption spectroscopy (XAS). Supports and pH > 13 strongly enhanced the precatalytic voltammetric charge of the Ni–Fe oxyhydroxide redox peak couple, shifted them more cathodically, and caused a 2–3-fold increase in the catalytic OER activity. Analysis of DEMS-based faradaic oxygen efficiency and electrochemical UV–vis traces consistently confirmed our voltammetric observations, evidencing both a more cathodic O_2 release and a more cathodic onset of Ni oxidation at higher pH. Using UV–vis, which can monitor the amount of oxidized $Ni^{+3/+4}$ *in situ*, confirmed an earlier onset of the redox process at high electrolyte pH and further provided evidence of a smaller fraction of $Ni^{+3/+4}$ in mixed Ni–Fe centers, confirming the unresolved paradox of a reduced metal redox activity with increasing Fe content. A nonmonotonic super-Nernstian pH dependence of the redox peaks with increasing Fe content—displaying Pourbaix slopes as steep as −120 mV/pH—suggested a two proton–one electron transfer. We explain and discuss the experimental pH effects using refined coupled (PCET) and decoupled proton transfer–electron transfer (PT/ET) schemes involving negatively charged oxygenate ligands generated at Fe centers. Together, we offer new insight into the catalytic reaction dynamics and associated catalyst redox chemistry of the most important class of alkaline OER catalysts.

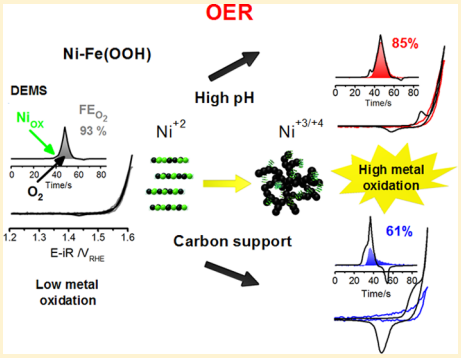

1. INTRODUCTION

The oxygen evolution reaction (OER) leading to formation of O_2 and the release of protons (H^+) and electrons (e^-) is a key reaction in the production of renewable fuels. Non-noble Ni–Fe oxide electrocatalysts have shown high catalytic activity in alkaline electrolytes,[1−13] applicable in electrolyzers[14] and in solar-water splitting devices.[15−18]

Fe impurities were first reported by Corrigan et al. to catalyze oxygen evolution in electrodeposited Ni–Fe(OOH) at comparably low overpotentials, observed as a "volcano" shaped activity trend following the Sabatier principle.[1,2] Utilizing X-ray photoelectron spectroscopy (XPS) in combination with a new purification method to eliminate Fe impurities present in the electrolyte, Trotochaud et al. confirmed that Fe was responsible for the observed "activation" behavior of NiOOH during anodic conditioning.[19,20]

Several studies concerning Ni–Fe catalysts deposited on carbon or high surface area supports have demonstrated superior catalytic activities in comparison to unsupported Ni–Fe catalysts.[10−12,21,22] Gong et al. demonstrated that solvothermally prepared Ni–Fe layered double hydroxide (LDH) supported on oxidized carbon nanotubes (CNTs) yielded higher activity than unsupported catalyst with a turnover frequency of 0.56 s^{-1} per total metal site at 300 mV overpotential (η) in 1 M KOH.[10] Qiu et al. investigated small sized Ni–Fe hydroxide nanoparticles (NPs) on Vulcan carbon support, which showed overpotentials in the order of 280 mV at 10 mA cm^{-2} in 1 M KOH.[11] Under the same conditions, Ma et al. showed that exfoliated Ni–Fe nanosheets on reduced

Received: November 28, 2016
Published: January 12, 2017

DOI: 10.1021/jacs.6b12250
J. Am. Chem. Soc. 2017, 139, 2070–2082

graphene oxide had an overpotential of 240 mV and an associated turnover frequency (TOF) of 0.1 s^{-1}.[23] Lu et al. electrodeposited Ni−Fe(OOH) catalyst on Ni foam with an overpotential of 215 mV; however, the reported TOF was only in the order of 0.075 s^{-1} at η = 400 mV.[22] Whether these measurable differences are caused largely by the exposed electrochemically accessible surface area, mass loading, or from other factors such as particle size effects and catalyst−support interactions still lacks systematic investigations.

The increasing number of reports have pointed toward substantial differences in the OER activity and the metal redox states during catalytic conditions. To achieve a fundamental understanding of the origins of the synergisms between Ni and Fe centers, an investigation of the possible impact of external factors such as catalyst support and measurement conditions will be crucial. This we will attempt to approach in this contribution.

To identify the local atomic structure in the OER active state in electrodeposited Ni−Fe(OOH) catalysts, X-ray absorption spectroscopy (XAS) under *operando* conditions by Friebel et al. disclosed metal redox states predominant as $Ni^{+3/+4}$ and Fe^{+3}.[24] The commonly observed anodic shift of the precatalytic redox wave assigned to $Ni(OH)_2 \rightarrow NiOOH$,[25,26] caused by Fe incorporation, was confirmed by Bates et al. as a stabilization of Ni^{+2} atoms to more anodic electrode potentials in mixed Ni−Fe catalysts.[27] However, a recent study from our workgroup has confirmed that Fe stabilizes low-valent Ni^{+2} atoms in mixed Ni−Fe centers also under OER catalytic potential.[27] To explain these conflicting reports, Fe was hypothesized to shift the stationary concentration of oxidized $Ni^{+3/+4}$ vs the reduced Ni^{+2} by impacting the oxygen evolution rate (k_{OER}) versus the metal oxidation rate ($k_{M,ox}$).[28] This could prevent oxidized $Ni^{+3/+4}$ species from accumulating to detectable levels.[28] A recent computational DFT+U study showed that Fe may induce electron transfer from Fe to Ni in mixed Ni−Fe centers, which stabilizes Ni^{+2} atoms and formation of Fe^{+4}.[29] The study also showed that the lowest energy configuration was very similar for different interlayer stacking and proton environments in NiOOH materials, which predicts that the local environment may be dependent on the species.[29] With this in mind, it is likely that different types of oxyhydroxide catalysts may have local environments that favor different metal redox states. This could help explain why a variation of Ni and Fe oxidation states in mixed Ni−Fe(OOH) catalysts has been reported to date.[24,27,28,30,31] An observation by Enman et al. was a poor correlation between the Ni redox peak and the catalytic OER activity in NiOOH doped with different metals (Mn, La, Ti, Ce, Fe).[32] This clearly demonstrates that the interpretation of the redox peak area in relation to the catalytic OER activity requires far more knowledge of the formal charge of the Ni at the impact of a second metal. What remains under debate is whether Ni or Fe is the active site. A DFT+U study pointed toward Fe as the most likely active site, since the OER intermediates showed most optimal binding energies resulting in a lower OER overpotential at a Fe site.[24]

Regarding pH dependence and the nature of the OER intermediates, Koper and co-workers recently identified "active oxygen" species forming under catalytic potential in Ni(Fe)-OOH catalysts using surface enhanced raman spectroscopy (SERS), which could be attributed to oxidic (NiO^-) or superoxidic ($NiOO^-$) species.[33,34] A decoupled OH^-/e^- elementary step occurring during the OER cycle was proposed in accordance with the observations and used as an argument to explain the strong pH dependence of the oxygen evolution activity.[35]

Here we present a systematic study of the influence of carbon support in solvothermally prepared Ni−Fe oxyhydroxide electrocatalysts, at various electrolyte pH and varying measurement conditions. We use a combination of standard electrochemical rotating disk electrode (RDE), physical characterization techniques (XRD, BET, TEM), *quasi-in situ* X-ray absorption spectroscopy (XAS), *operando* differential electrochemical mass spectrometry (DEMS), and *in situ* UV−vis spectroelectrochemistry to evaluate quasi-stationary and steady state levels of volatile products and spectroscopic signatures of redox-active metals. We aim to track catalyst redox state changes during oxygen evolving conditions. Several key parameters were examined in an attempt to establish correlations between catalytic activity, O_2 evolution, and metal redox processes.

2. EXPERIMENTAL SECTION

2.1. Synthesis. Ni−Fe catalysts were synthesized by microwave assisted autoclave synthesis under solvothermal conditions.[12] Desired ratios of Ni and Fe were obtained by mixing different stochiometries of 0.1 M $Ni(NO_3)_2 \times 6H_2O$ (99.999% trace metals basis, Aldrich) and 0.1 M $Fe(acac)_3$ (99.5% trace metal basis, Aldrich) in benzyl alcohol (puriss., 99−100.5%, Aldrich) to a final concentration of 22 mM, and addition of 10 mM 1,2-benzenediol (purity grade, Sigma-Aldrich), and a total reaction volume of 20 mL. All chemicals were used as received without further purification. The reaction mixtures were sealed in special autoclave vials (Anton Paar) and heated in a Monowave 300 (Anton Paar). The mixtures were heated to 190 °C with a ramping step of 16.5 °C/min, and held for 15 min. Carbon supported catalysts were prepared by addition of 90 wt % Vulcan XC-72r (Cabot) after synthesis when the mixtures had cooled down. The catalysts were added to the carbon support by dropping to a carbon slurry dissolved in high purity ethanol under sonication. The catalyst−carbon mixture was left for an additional 30 min of sonication and afterward stirring for 24 h. The product was collected and washed five times with high purity ethanol containing 10% Milli-Q water (>18 MΩ cm) using repeated centrifugation at 7500 rpm for 10 min. The samples were freeze-dried and stored as powders under an inert atmosphere until use.

2.2. Elemental Analysis. The metal content of Ni and Fe was analyzed by inductively coupled plasma-optical emission spectroscopy (ICP-OES) using a Varian 715-ES spectrometer with a CCD detector. Samples were digested in acid (HNO_3:H_2SO_4:HCl in a 1:1:3 ratio) and heated using microwave irradiation to 180 °C for 15 min, with a ramping step of 15.5°/min. The samples were diluted with Milli-Q water (>18 mΩ cm) to reach an appropriate emission intensity. Standards with a known concentration were coanalyzed with the samples.

Metal contents analyzed after electrochemical conditioning were analyzed using total reflection X-ray fluorescence (TXRF) spectroscopy. Electrodes were dissolved in a volume of 300 μL of HCl (37%, Merck) using sonication. Additions of Ga standard (Merck) of a concentration of 1 mg/L allowed for quantitative determination of the metal content. The analysis was acquired using a Bruker S2 Picofox spectrometer at 40 kV using an XFlash Si-drift detector.

2.3. Physical Characterization. X-ray diffraction (XRD) was acquired on a Bruker D8 Advance diffractometer with Cu Kα radiation and a Lynx Eye detector. Samples were analyzed between 10 and 80° 2θ, with a step size of 0.04° and a collection time of 6 s. Data analysis was carried out using MDI Jade 9.

Transmission electron microscopy (TEM) was carried out using a FEI Tecnai G^2 Microscope 20 S-Twin with a LaB_6 cathode at 200 kV accelerating voltage (ZELMI Centrum, Technical University of Berlin). The microscope was equipped with an energy dispersive X-ray (EDX) detector for elemental analysis. Catalyst powders were

DOI: 10.1021/jacs.6b12250
J. Am. Chem. Soc. 2017, 139, 2070−2082

dispersed in 2-propanol by ultrasonication and drop-dried onto Cu grids. Analysis was carried out using software from ImageJ.

Brunauer Emmet Teller (BET) N_2 adsorption isotherms were used to determine specific surface area and were measured using a Quantachrome Autosorb-1-C. The samples were outgassed in a vacuum at 70 °C for ∼22 h prior to the measurements. The adsorption was measured at 77 K in a relative pressure range $\left(\frac{\rho}{\rho_0}\right)$ of 0.08−0.3.

2.4. Electrochemical Characterization. Electrochemical characterization was carried out in a standard three-electrode rotating disc electrode (RDE) setup from Pine Instruments. Polished glassy carbon (GC) electrodes were used as working electrodes (Ø = 5 mm, Pine Instruments) and a Pt mesh was used as a counter electrode, measured versus a reversible hydrogen reference electrode (RHE). All measurements were controlled using a Gamry Reference 600 potentiostat in 0.1, 0.5, and 1 M KOH (semiconductor grade, 99.99% trace metals basis, Sigma-Aldrich). Cyclic voltammograms were collected at a rotation speed of 1600 rpm and steady-state measurements at 2200 rpm unless otherwise stated. Catalyst inks were prepared by dispersing 5 mg of the catalyst powders in a mixture of 1000 μL of Milli-Q, 1500 μL of 2-propanol, and addition of 20 μL of Nafion (5 wt %). The inks were homogeneously dispersed by ultrasonication for 20 min and drop-casted on the GC electrodes. To make up a final metal loading of 10 μg cm^{-2}, ca. 5−10 μL of ink was drop-casted on the electrodes. Varying metal loadings were achieved by varying the amount of ink drop-casted on the electrodes. The total metal contents of Ni+Fe were determined by elemental analysis.

2.4.1. In Situ UV−vis Spectroelectrochemistry. UV−vis spectra were collected using a UV/vis/NIR spectrometer from Avantes (AvaLight-DH-S-BAL) equipped with a deuterium and halogen lamp and a light guide. The spectrometer was connected via fiber optic cables to the electrochemical cell. Spectra were collected between 250 and 900 nm with a time resolution of 400 ms. The electrochemical cell constituted a 1 cm quartz cuvette, a leak free Ag/AgCl reference electrode with a Ø = 1 mm shaft (Warner Instruments), and a Pt mesh counter electrode placed along the sides of the beam path. All potentials are reported versus the reversible hydrogen electrode (E_{RHE} = 0.198 V + 0.059 V × pH). Fluorine doped tin oxide (FTO) electrodes (Sigma-Aldrich) were used as working electrodes, precut to fit into the cuvette. The electrodes were cleaned prior to the measurements in high purity ethanol and afterward rinsed with Milli-Q water using sonication. Electrolyte was prepared from semiconductor grade KOH pellets (99.99% trace metals basis, Sigma-Aldrich) and diluted with Milli-Q water to 0.1, 0.5, and 1 M KOH. Measurements of NiOOH catalyst were carried out in Fe-free KOH which had been purified according to a previously reported method.[19] The UV−vis spectrum was blanked versus an empty FTO substrate.

2.5. Mass Spectrometry and Gas Chromatography. *2.5.1. Differential Electrochemical Mass Spectrometry.* Differential electrochemical mass spectrometry (DEMS) was measured in a dual thin layer electrochemical flow cell partly based on the design described elsewhere.[36] DEMS was recorded in 0.1, 0.5, and 1 M KOH electrolytes. The electrochemistry was controlled using a BioLogic potentiostat, a leak-free Ag/AgCl as a reference electrode (Warner Instruments), and a Pt mesh as a counter electrode. The reported cell voltages are reported on the RHE scale (E_{RHE} = 0.198 V + 0.059 V × pH); the real offsets were determined in each electrolyte by calibration against a Pt working electrode in H_2 saturated electrolyte. The DEMS cell was connected to a mass spectrometer (QMS 200, Pfeiffer Vacuum) via a 150 μm thick microporous PTFE membrane with 30 nm pore size (Cobetter). Two turbomolecular pumps (HiPace 80) were operating at 10^{-6} mbar. Catalysts were drop-casted onto polished GC electrodes (Ø = 5 mm, Pine Instruments) to make up a total metal loading of ∼10 μg of Ni+Fe cm^{-2}. CVs were recorded by potential cycling between ∼1 and 1.75 V_{RHE} (before *i*R-comp). The scan limits varied slightly for the different electrolyte pHs to account for differences in resistance and catalytic activity. The catalysts were first preconditioned at a scan rate of 100 mV/s for ∼200 cycles until a steady-state CV had been reached. The mass spectrometric ion currents for each volatile product *j* ($i_{MS,j}$) were converted into the corresponding faradaic current contributions, $i_{F,j}^{DEMS}$, using a catalyst-specific calibration factor K_j^{**}. Values for K_j^{**} were obtained for each catalyst in separate steady-state measurements (see Table S1a) of mass spectrometric ion currents and faradaic currents according to

$$K_j^{**} = \frac{i_{MS,j}}{i_F^{100\%FE}} \tag{1}$$

Integrating the voltammetric faradaic currents and the mass spectrometric ion currents to obtain Q_F and $Q_{MS,j}$, respectively, allows for determination of a species-specific faradaic efficiency (FE) according to

$$FE\ (\%) = \frac{Q_{MS,j}}{Q_F \cdot K_j^{**}} \times 100 \tag{2}$$

2.5.2. Headspace Mass Spectrometry and Gas Chromatography. Online mass spectrometry was measured in a gas-tight electrochemical cell in a steady flow of 5 sccm N_2 controlled by flow meters (El-flow, Bronkhorst). The mass spectrometer (Pfeiffer Omnistar GSD 301) was coupled to the gas outlet for continuously monitoring volatile gases in the N_2 stream. All measurements were carried out in 0.1 M KOH (semiconductor grade, Sigma-Aldrich) used as received, with an RHE reference electrode and a Gamry reference 3000 potentiostat. A Pt mesh was used as a counter electrode separated by a glass frit to avoid H_2 entering the gas stream. Catalysts were drop-casted onto carbon fiber paper (AvCarb P50T, Ballard Power Systems) with an area of ∼2 cm^2 to make up a total metal loading of ∼30 μg_{Ni+Fe} cm^{-2}. Chronopotentiometric (CP) steps were applied between 0.25 and 10 mA cm^{-2}. Gas chromatography (GC) samples were regularly taken out from the gas phase using a gas-tight syringe (Hamilton). The gas was injected into a GC-2014 chromatograph (Shimadzu) equipped with a Molsiev 13× column and a thermal conductivity detector (TCD). The theoretical volume % of the volatile product *j* could be determined in the headspace according to eqs 3 and 4

$$\dot{v}_j = \frac{i \cdot A \cdot V_m}{z \cdot F} \tag{3}$$

$$v_{j,thr} = \frac{\dot{v}_j}{\dot{v}_j + \dot{v}_{N_2}} \tag{4}$$

where $\dot{v}_j$ is the theoretical volumetric flow of product *j* at 100% faradaic selectivity, $\dot{v}_{N_2}$ is the applied flow of N_2, $v_{j,thr}$ is the theoretical volume % of product *j*, *i* is the applied current density, *A* is the electrode area, V_m is the standard molar gas volume, and *F* is the Faraday constant.

The faradaic efficiency of product *j* in the headspace (FE_{HS-MS}) could be determined from the mass spectrometric detected volume % of product *j* ($v_{j,MS}$) in the theoretical volume % of product *j* according to eq 5

$$FE_{HS-MS} = \frac{v_{j,MS}}{v_{j,thr}} \times 100 \tag{5}$$

2.6. X-ray Absorption Spectroscopy (XAS). *Quasi-in situ* X-ray absorption spectroscopy (XAS) was measured of catalysts drop-casted on polished GC electrodes with an area of ∼1.5 cm^2. Electrodes were assembled in special sample holders. A Pt mesh was used as a counter electrode and a reversible hydrogen reference electrode connected via a Luggin capillary. Samples were conditioned at 1.63 V_{RHE} for 30 min as a conditioning step, and subsequently cooled under the applied potential using liquid N_2 (freeze quenching) according to a reported method.[28,37,38] XAS was measured at the Ni and Fe *K*-edges at the KMC-1 beamline at the BESSY-II synchrotron (Helmholtz-Zentrum Berlin, Germany) at a temperature of 20 K controlled by a liquid-helium cryostat. Spectra were collected in the fluorescence mode using a 13-element energy-resolving Ge detector (Canberra) by selecting the Kα fluorescence of the Ni and Fe *K*-edges. The k^3 weighted EXAFS spectra were simulated in *k*-space using E_0 = 8333 eV for Ni and E_0 = 7115 eV for Fe, an amplitude reduction factor (S_0^2) of 0.85, and a *k*-range of 20−760 eV corresponding to 2.3−14 Å^{-1}. Phase functions

DOI: 10.1021/jacs.6b12250
J. Am. Chem. Soc. 2017, 139, 2070−2082

were generated using FEFF software version 9.1 with self-consistent field.[39,40] In-house software (SimX) were used for the simulations. The parameters were optimized as described elsewhere.[28]

3. RESULTS AND DISCUSSION

3.1. Physical Characterization of Ni−Fe Catalysts. Unsupported mixed Ni−Fe(OOH) nanoparticle electrocatalysts with various stoichiometric compositions were synthesized according to a previously reported solvothermal method (see Figure 1a).[12,28] To investigate the influence of a carbon catalyst

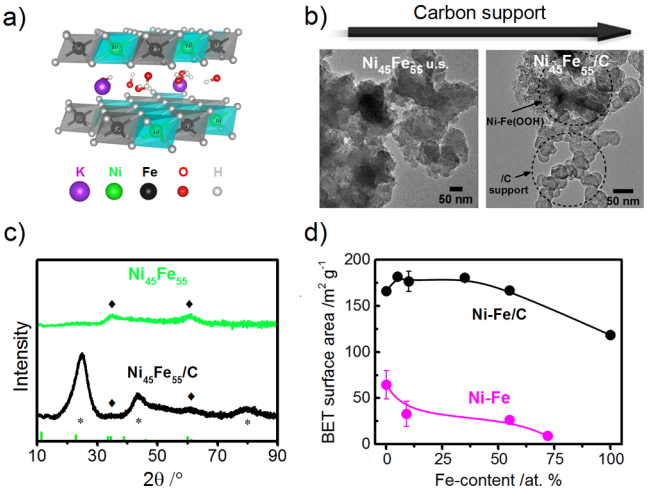

Figure 1. (a) Structural model of a small sheet of Ni−Fe(OOH), synthesized solvothermally, with intercalated water and K^+ (cif 9012316). (b) TEM images of unsupported $Ni_{45}Fe_{55}$ and carbon supported $Ni_{45}Fe_{55}$/C catalysts (supported on Vulcan XC-72r). (c) Powder X-ray diffraction (XRD) of the $Ni_{45}Fe_{55}$ and $Ni_{45}Fe_{55}$/C catalysts. The bottom lines show the powder diffraction profile of α-$Ni(OH)_2$ (green, # 00-038-0715). The tilted squares mark the reflections of the catalyst and the asterisks the reflections of the Vulcan XC-72r carbon support. (d) BET surface area obtained from the N_2 adsorption isotherm of unsupported Ni−Fe and carbon supported Ni−Fe/C catalysts with varying Ni:Fe compositions. All atomic compositions are given as atomic % Fe, determined by ICP-OES. The error bars are given as standard errors.

support, the unsupported Ni−Fe catalysts were immobilized on Vulcan XC-72r post synthesis (referred to as "Ni−Fe/C"), not to alter the catalyst particle size.

Transmission electron microscopy showed that the Ni−Fe/C catalysts exhibited a similar morphology to the unsupported Ni−Fe catalysts (Figure 1b). The oxyhydroxide catalysts were immobilized on top of the carbon support to an extent of 10 wt % metal loading. There were also visible spots with a lower coverage of catalyst showing a more exposed carbon structure (Figure 1b). X-ray diffraction confirmed an amorphous character of both the unsupported and carbon supported Ni−Fe catalysts (Figure 1c). Reflections at 34 and 42° 2θ matched well with the (1 0 1) and (1 1 0) reflections of α-$Ni(OH)_2$.[19,41] The (0 0 2) and (1 0 0) reflections of the carbon support at 24 and 42° 2θ were overlapping with the (0 0 6) reflection of the oxyhydroxide structure, which are generally weak in turbostratic $Ni(OH)_2$ materials.[42,43] Upon increasing Fe content, the XRD reflections of the Ni−Fe/C catalysts decreased in intensity in accordance with earlier reports of Fe insertion in unsupported Ni−Fe catalysts (Figure S1).[28]

The BET surface area was investigated using the N_2 adsorption isotherm (Figure 1d). Independent of the Ni:Fe composition, there was a low extent of mesoporosity and micropososity in these materials. The BET surface area of the $Ni_{45}Fe_{55}$/C catalyst amounted to 182 m^2/g, whereas the unsupported $Ni_{45}Fe_{55}$ catalyst showed a lower surface area of 27 m^2/g, similar to previous established BET surface areas of Ni−Fe oxide catalysts.[8] The high BET areas of the Ni−Fe/C catalysts were derived from the carbon support, which had a BET surface area of 187 m^2/g. Despite the offset between unsupported and carbon supported Ni−Fe catalysts, there was a consistent trend with larger BET surface area at high Ni content. This suggests that the densities of the N_2 adsorption sites in $Ni(OH)_2$ and FeOOH are different. Whether a correlation between the BET surface area and the electrochemically active surface area prevails in mixed Ni−Fe catalysts has been under discussion.[8,31] Since our catalysts show interfacial faradaic charge-transfer reactions which are affected by the Ni:Fe stoichiometry,[28] an accurate determination of the double layer capacitance was challenging.[3,44] For the moment, we could not establish a reliable estimate of the catalytically available surface sites in our Ni−Fe catalysts among the full range of Ni:Fe compositions. Therefore, a possible correlation to the BET surface area will require further investigations.

3.2. Electrocatalytic Oxygen Evolution Activity. Carbon supported Ni−Fe/C catalysts consistently showed a 2−3-fold higher catalytic activity compared to unsupported Ni−Fe catalysts (see Figure 2a,b). Lower limit turnover frequencies (TOFs) were estimated from CVs recorded at 2 mV/s, based on the total moles of metal (Ni+Fe) deposited on the electrodes (TOF_{Ni+Fe}), determined by ICP-OES. The current densities derived from the CVs were in good agreement with steady-state measurements (Figure S2). The highest TOFs in 0.1 M KOH were observed for the $Ni_{45}Fe_{55}$ and $Ni_{45}Fe_{55}$/C catalysts and determined to 0.10 and 0.20 s^{-1} (Figure 2c). By increasing the electrolyte concentration from 0.1 to 1 M KOH (pH 13 to 13.87), an additional activity boost was observed (Figure 2b). Higher electrolyte pH also slightly shifted the activity maximum toward higher Ni content.

The TOFs of the $Ni_{65}Fe_{35}$ and $Ni_{65}Fe_{35}$/C catalysts in 1 M KOH peaked at 0.14 and 0.34 s^{-1}, clearly exceeding the top performing 55 at. % Fe materials in 0.1 M KOH. More importantly, the redox charge under the redox peak assigned to the $Ni(OH)_2 \rightarrow NiOOH$ oxidation became significantly larger in either 1 M KOH or in the presence of the carbon support (Figure 2d). The latter can be explained by a better metal oxide particle dispersion and more exposed catalytic sites, while the effect of pH suggests the participation of protons in the rate-determining step.

Tafel slopes ranged around ~60 mV dec^{-1} for Ni catalysts and ~40 mV dec^{-1} for mixed Ni−Fe catalysts; however, they were consistently lower for supported Ni−Fe/C catalysts (Figure S3).

Short-term OER stability comparisons of Ni−Fe and Ni−Fe/C catalysts were investigated in 0.1 M KOH. Both catalysts showed good cycling stability with only an ~10 mV increase in overpotential after 1000 potential cycles (Figure 3). After 20 h of bulk electrolysis at a constant current density of 10 mA cm^{-2}, however, there was a much larger, ~30 mV, increase in overpotential (Figure S4). It is possible that potential cycling leads to reactivation effects associated with redeposition of leached metal ions or causes a lower stress due to the introduction of a resting phase at noncatalytic potential. It is possible that oxygen bubbles can be removed which is not possible during galvanostatic polarization. An estimation of the

DOI: 10.1021/jacs.6b12250
J. Am. Chem. Soc. 2017, 139, 2070−2082

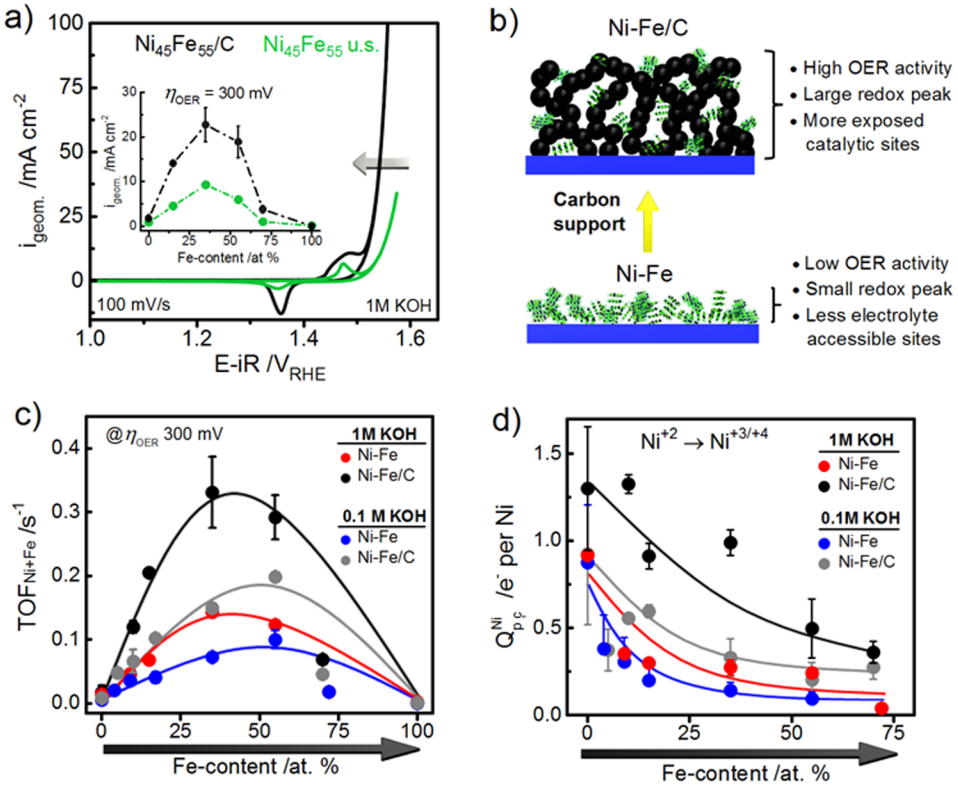

Figure 2. (a) CVs of unsupported ("u.s.") and carbon supported ("/C") Ni−Fe catalysts in 1 M KOH measured at a scan rate of 100 mV/s. The inset shows the geometric current density as a function of Fe content at η = 300 mV. (b) Schematic representation of the effects of a carbon support. (c) Lower limit TOFs on the basis of the total metal loading of Ni+Fe (TOF_{Ni+Fe}) as a function of Fe content, estimated at η = 300 mV from CVs measured at 2 mV/s. (d) Redox electrons (e^- per Ni) determined from integration of the cathodic redox peak, using CVs recorded at a scan rate of 10 mV/s. The measurements were carried out at a fixed geometric metal loading of 10 μg Ni+Fe cm^{-2}, determined by ICP-OES.

amount of catalyst material metal left on the electrodes after 1000 potential cycles showed a loss of ∼38% of the total metal content for both $Ni_{45}Fe_{55}$ and $Ni_{45}Fe_{55}$/C catalysts (see Figure S5).

3.2.1. Catalyst Loading Effects on the OER Activity. OER activity measurements of unsupported Ni−Fe ("u.s.") and carbon supported ("/C") catalysts were carried out as a function of metal loading (Figure 4a and Figure S6a−c). As exemplified by the $Ni_{45}Fe_{55}$/C catalyst, the catalytic geometric current density as well as TOF values of the supported catalyst increased nearly proportionally with the metal loading before stabilizing at higher loadings regardless of pH (Figure 4b). Conversely, the unsupported $Ni_{45}Fe_{55}$ catalyst showed a less steep increase in the current and a monotonic decrease in TOF with higher loading at either pH. In recent work by Batchellor et al., a comparison of continuous and pulse-electrodeposited Ni−Fe(OOH) catalysts showed a similar trend to what was observed here.[3] The continuously deposited catalyst exhibited a descending TOF, whereas the pulsed deposited catalyst showed an increasing TOF with loading.[3] This was explained as a better connectivity and minimal contributions of electrical, ionic, or mass transfer resistances in the catalytic film.[3] Our comparative trends in TOF values for supported and unsupported solvothermal Ni−Fe(OOH) catalysts support this hypothesis: the supported catalysts show improved particle dispersion on a conductive carrier and hence should suffer less from mass transport and charge transport resistances despite thicker films at higher loadings.[12] Data for the supported $Ni_{45}Fe_{55}$ catalyst further evidence that a significantly higher OER activity can be maintained at high catalyst loadings by increasing the electrolyte pH from 13 (0.1 M KOH) to ∼14 (1 M KOH). A number of different explanations can account for this. Higher pH at larger particle dispersion boosts the local buffer capacity, preventing a drop in local pH and thus effective overpotential, caused during high oxygen evolution rates as a consequence of OH^- depletion. Also, better particle dispersion generates a larger portion of electrolyte accessible metal sites, which would translate in higher TOF values. Finally, high ionic electrolyte and electronic conductivity may benefit rate determining proton transfer kinetics.[19,44]

The faradaic charge under the $Ni(OH)_2$ redox peak in Figure S6d followed closely the trends of the TOF values with increasing metal loadings. The number of redox electrons (transferred per Ni atoms) rose significantly with the support, jumping from 0.2 e^- to as high as 0.75 e^- per Ni atom for the unsupported $Ni_{45}Fe_{55}$ and the supported $Ni_{45}Fe_{55}$/C catalyst, respectively. This lends support to the enhanced metal center accessibility hypothesis to explain the significantly improved OER activity. For the supported catalysts, the number of redox electrons per Ni increased more significantly when going from pH 13 to pH ∼14. This finding precludes conclusions that the enhanced TOF values are largely controlled by ionic conductivity or local buffer capacity. The reason for a generally lower TOF at low catalyst loadings may be explained if enhanced activity can be achieved when edge sites are in close contact. We note that, regardless of support or pH, the total faradaic redox charge in mixed Ni-Fe catalysts remained much smaller compared to the Ni-only catalyst (1.5 e^- per Ni atom), in agreement with earlier results where Fe was found to mute the redox activity of Ni.[28] Thus, neither pH nor support appear

DOI: 10.1021/jacs.6b12250
J. Am. Chem. Soc. 2017, 139, 2070−2082

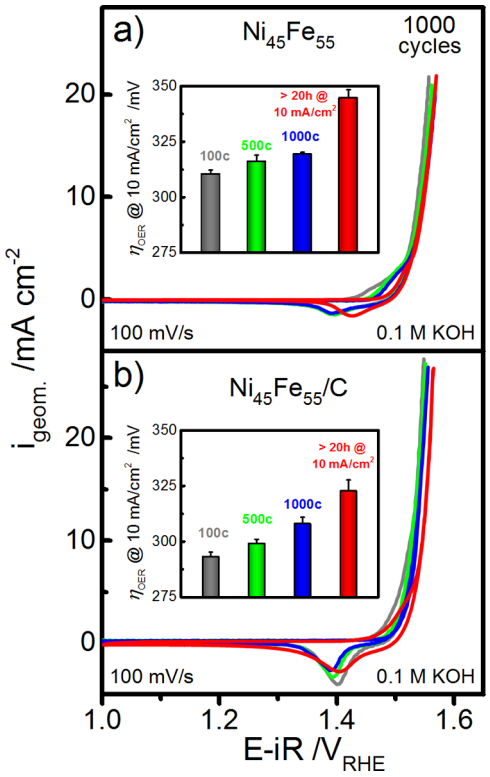

Figure 3. Stability performance up to 1000 cycles between 1 and 1.6 V_{RHE} at a scan rate of 100 mV/s and steady-state chronopotentiometric measurements at 10 mA cm^{-2} for 20 h: (a) unsupported $Ni_{45}Fe_{55}$; (b) carbon supported $Ni_{45}Fe_{55}$/C. CVs are displayed after 100 cycles (gray), 500 cycles (green), and 1000 cycles (blue), and after steady-state measurements at 10 mA cm^{-2} for 20 h (red). The insets show the associated OER overpotentials.

to fully recover the metal redox activity in mixed Ni-Fe catalysts to the levels observed for the Ni-only catalysts.

3.3. DEMS-Derived Charge Efficiency during Oxygen Evolution. To track the distribution of faradaic charge injected into formation of products (O_2 release) and into catalyst redox processes (change in metal redox states), we used differential electrochemical mass spectrometry (DEMS). The measurements were carried out in a dual thin-layer electrochemical flow cell based on a similar design reported elsewhere.[45] Oxygen evolution activities were measured for unsupported $Ni_{45}Fe_{55}$ and supported $Ni_{45}Fe_{55}$/C catalysts. To gain a deeper understanding of the effects of carbon support and electrolyte pH on the charge efficiency, measurements were carried out in 0.1, 0.5, and 1 M KOH electrolytes (pH 13, 13.7, and 13.9, respectively). The catalysts were first cycled in 0.1 M KOH until a stable CV had been reached (~200 cycles), and next switched to 0.5 M KOH, and thereafter to 1 M KOH, without removing or changing the electrode. The faradaic efficiencies of O_2 (FEO_2) were calculated using a sensitivity factor (K^*) to convert the ion currents to corresponding DEMS-derived faradaic currents ($i_{F,O2}^{DEMS}$), the integral charge of which was subsequently divided by the total faradaic charge derived from voltammetry. The absolute levels of O_2 were also confirmed close to 100% in the steady state using online mass spectrometry coupled to gas chromatography (GC) where volatile species were sampled in the headspace in a steady flow of 5 sccm N_2 (Figure S7 and Table S1b). Cyclic scans of the voltammetric faradaic currents (black lines) and the O_2 DEMS-derived faradaic currents ($i_{F,O2}^{DEMS}$) (colored lines) are compared in the potential domain in Figure 5a–f. The insets show both data sets in the time domain.

The colored areas in the insets of Figure 5a–f represent the integral of ($i_{F,O2}^{DEMS}$) corresponding to the charge of the evolved oxygen, while the black lines denote the total faradaic voltammetric current (i_F).

In 0.1 M KOH, The faradaic O_2 efficiency was estimated to 93% O_2 for the unsupported $Ni_{45}Fe_{55}$ catalyst and to 81% for the supported $Ni_{45}Fe_{55}$/C catalyst, indicating a lower level of catalyst redox activity in the unsupported catalyst. By gradually increasing the pH by changing the electrolyte concentration from 0.1 M → 0.5 M → 1 M KOH, the apparent redox charge associated with processes other than oxygen evolution increased significantly, and the FEO_2 decreased from 93% → 86% → 85% for $Ni_{45}Fe_{55}$ catalyst and from 81% → 61% → 55% for the $Ni_{45}Fe_{55}$/C catalyst in the corresponding electrolytes (see overview in Figure 5g). We also note that O_2 release did not set off before near completion of the catalyst-related redox wave. Our data establish for the first time a clear reemergence of catalyst-related (metal and ligand) redox processes with increasing pH and with increasing catalyst dispersion on a support.

Evaluating the faradaic O_2 efficiency from Figure 5 omitting the catalyst redox charge from the total faradaic charge, it approached 100% within the error of the peak deconvolution for the unsupported $Ni_{45}Fe_{55}$ catalyst (Figure S8). For the $Ni_{45}Fe_{55}$/C catalysts on the contrary, the efficiency was much lower despite attempts to eliminate the charge associated with the redox peak. This may inflict a contribution from a carbon

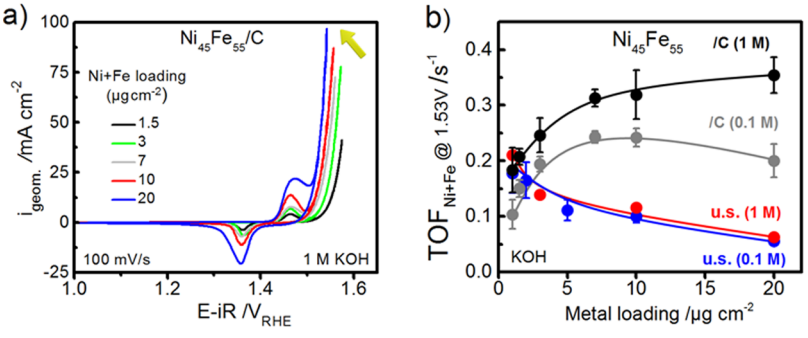

Figure 4. Measurements at various metal loadings of the $Ni_{45}Fe_{55}$ and $Ni_{45}Fe_{55}$/C catalysts ranging from 1 to 20 μg Ni+Fe cm^{-2}. (a) CVs at 100 mV/s of carbon supported $Ni_{45}Fe_{55}$/C catalyst in 1 M KOH. (b) Turnover frequency (TOF) of unsupported $Ni_{45}Fe_{55}$ and $Ni_{45}Fe_{55}$/C in 0.1 and 1 M KOH. (b) CVs at 100 mV/s of $Ni_{45}Fe_{55}$/C in 1 M KOH.

DOI: 10.1021/jacs.6b12250
J. Am. Chem. Soc. 2017, 139, 2070–2082

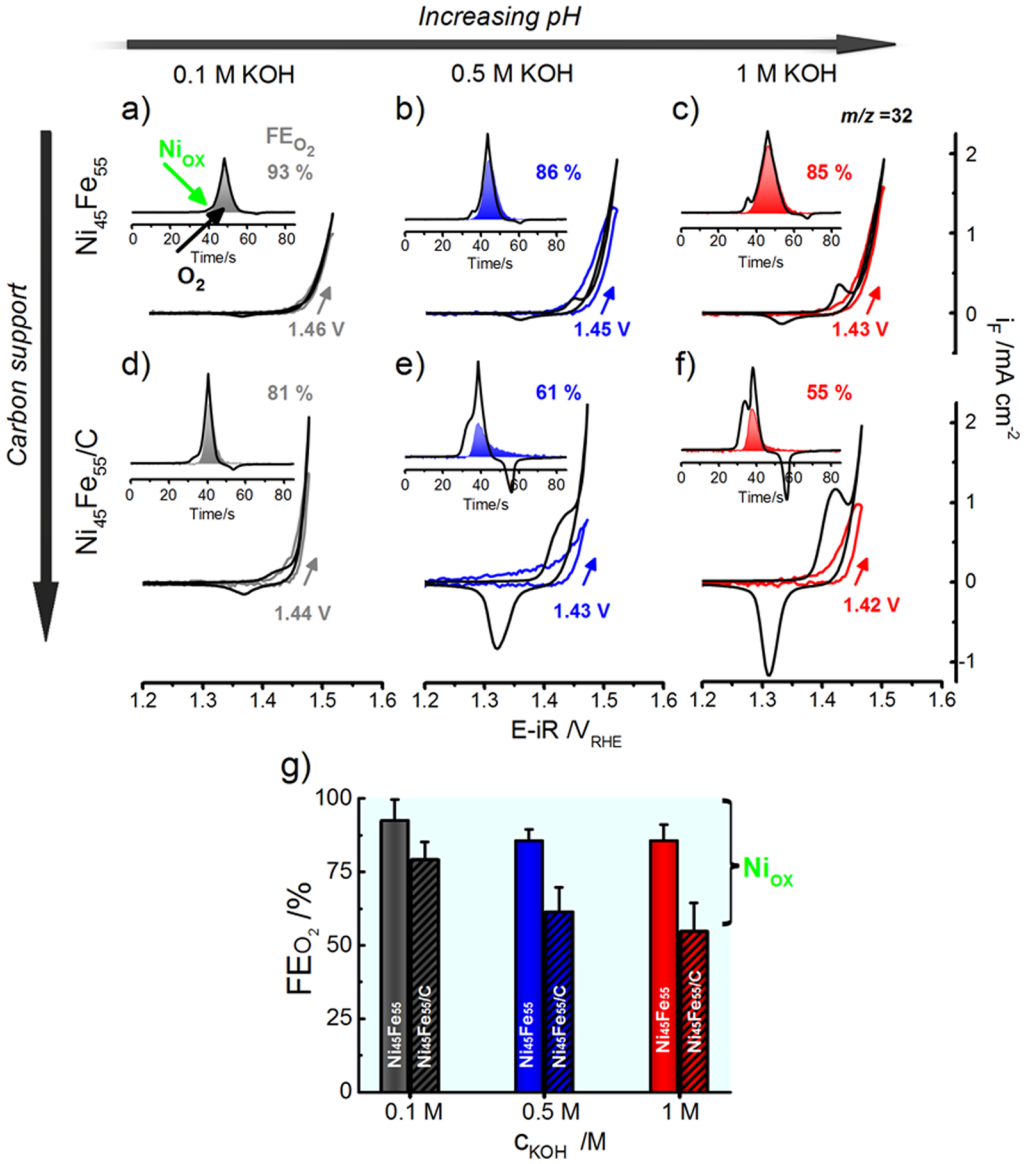

Figure 5. Differential electrochemical mass spectrometry (DEMS) measured in an electrochemical flow cell. Presented CVs were measured at a scan rate of 10 mV/s. The electrolyte was sequentially switched from 0.1 → 0.5 → 1 M KOH. (a–c) Unsupported $Ni_{45}Fe_{55}$ catalyst in 0.1 M KOH (gray), 0.5 M KOH (blue), and 1 M KOH (red). (d–f) Carbon supported $Ni_{45}Fe_{55}$/C catalyst in the corresponding electrolyte concentrations as shown in parts a–c. The insets show the CVs in the time domain. The time scales are not guaranteed entirely corrected for a time drift and inserted shifts due to ohmic resistances and reference electrode shifts associated with the different electrolyte pH. The current densities recorded at the potentiostat (i_F) are shown as black curves. The mass spectrometric faradaic ion currents of O_2 (m/z 32), $i_{F,O2}^{DEMS}$, are shown as colored lines or areas. The inset numbers indicate the faradaic efficiency O_2 (FEO_2). Potential values at the arrows at the bottom indicate the OER onset potential from the DEMS trace. (g) FEO_2 estimated for the catalysts shown in parts a–f by inclusion of the entire redox peak area (denoted Ni_{OX}). Redox charge and FEO_2 estimated by exclusion of the redox peak area are shown in Figure S8.

corrosion process in addition to the catalyst redox charge. We emphasize that we could not detect any indication of CO_2 of the supported catalysts judged from the absence of signal from CO_2 (m/z 44); see Figure S9. This fact does not exclude that CO_2 is formed, since it will escape detection under alkaline conditions (pH 13–14) due to the reaction between OH^- and CO_2 to form dissolved carbonates. In an earlier study from our workgroup, we showed that CO_2 could be detected in phosphate buffer pH 7 and borate buffer pH 9.2 of the carbon supported $Ni_{65}Fe_{35}$/C catalyst.[12] It should therefore be kept in mind that the lower faradaic efficiency observed of the Ni–Fe/C catalysts may partly come from a carbon corrosion process and not solely from an enhanced metal redox process. Further investigations will be needed to assess the contribution of carbon corrosion at pH 13–14.

Our DEMS charge efficiency analysis evidences that both carbon support and higher pH enhance catalyst metal redox processes, however in distinctly different ways. In accordance with the Tafel plot analysis of Figure S3, the carbon support shifts and strongly enhances the catalyst redox wave together with the oxygen evolution onset, resulting in a greatly enhanced OER activity and TOF. The pH value shifts the catalyst redox wave cathodically, which also increases in magnitude, and lowers the onset potential of the OER (see Figure 5). Higher pH coupled with a support combine both effects. These findings definitively exclude any simple masking of voltam-

DOI: 10.1021/jacs.6b12250
J. Am. Chem. Soc. 2017, 139, 2070–2082

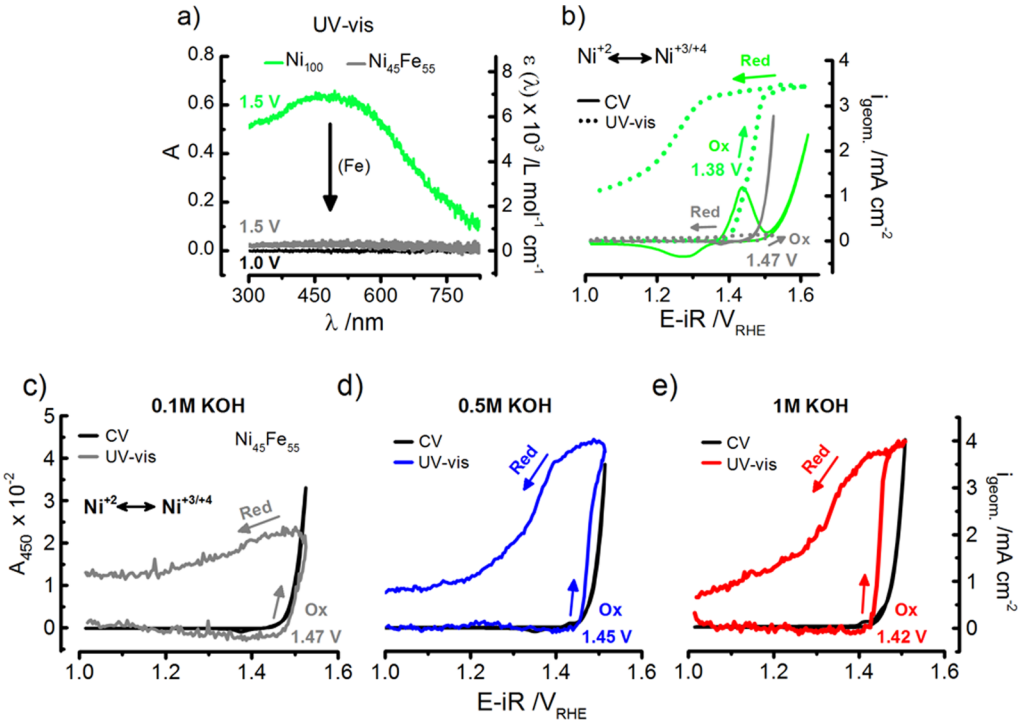

Figure 6. *In situ* UV−vis spectroelectrochemistry: (a) UV−vis absorption spectra of unsupported Ni(OOH) and $Ni_{45}Fe_{55}$(OOH) catalysts at 1.5 V_{RHE} in 0.1 M KOH. The black curve shows the spectral baseline at 1.0 V. The right axis shows the molar extinction coefficient (ε). (b) UV−vis spectra monitored at Abs_{450} (λ_{450nm}) during potential cycling of Ni and $Ni_{45}Fe_{55}$ catalysts in 0.1 M KOH. The solid lines show faradaic current density (i_{geom}, right axis), the dotted lines the absorption (left axis). (c−e) UV−vis spectra at A_{450} during potential cycling of the $Ni_{45}Fe_{55}$ catalysts in different electrolyte concentrations, consecutively switched from 0.1 M → 0.5 M → 1 M KOH. Catalyst loadings were kept constant at ∼5 μg cm^{-2} Ni. The CVs were recorded at 10 mV/s; the second cycle is shown. Potential values at the bottom in parts c−d indicate the onset potential of spectral fingerprints linked to Ni redox activity.

metric redox processes of the catalyst by the oxygen evolution onset. The support-induced increase in catalyst particle dispersion, on the other hand, causes (i) better charge transport and (ii) the number of electrolyte-accessible Ni/Fe/ligand centers to increase sharply. The number of electrochemically accessible metal/oxygen centers, in turn, directly controls the observed kinetic OER rate at a given overpotential, the change of that number will potentially affect the apparent Tafel slope. We note the presence of a cathodic "tail" during O_2 release on the $Ni_{45}Fe_{55}$ catalysts. This ion current tail is absent on less roughened surfaces such as polycrystalline Pt or even in IrO_x catalysts.[46] It was also discernible in previous investigations of unsupported Ni−Fe(OOH) catalysts with various compositions.[28] We speculate that this delayed O_2 release could reflect a kinetic- or diffusion-limited release of O_2.

In summary, our DEMS experiments suggest a strong dependence of the degree of catalyst redox activity, associated with the population of preactive metal/oxygen centers, on electrolyte pH and catalyst dispersion. Catalyst redox activity directly influences the catalytic OER activity.

3.4. Tracking Metal Redox States Using *In Situ* UV−vis Spectroscopy. *In situ* UV−vis spectroelectrochemistry was used to track the metal oxidation processes in NiOOH and the unsupported $Ni_{45}Fe_{55}$(OOH) catalysts and to compile findings in the DEMS experiments in a previous section regarding the onset of the metal redox process and possible masking inside the OER current. Measurements were carried out using a quartz cuvette, and catalysts were drop-casted on transparent FTO electrodes. Application of an OER catalytic potential induced a strong characteristic coloration of the Ni(OOH) catalyst, which was linked to the emergence of a broad spectral absorption band slightly above 450 nm (A_{450}); see Figure 6a.[17,26] The absorption band is assumed to be related to the Ni charge transfer processes, since no spectral changes were visible in the FeOOH catalyst or of an empty FTO electrode upon application of potential in the OER regime (see Figure S10). The observed absorption can therefore directly and unambiguously be linked to changes in the electrochromic properties of Ni. To cross-check the effect of Fe doping on the fingerprint spectral changes of the Ni catalyst, the unsupported $Ni_{45}Fe_{55}$ catalyst was investigated keeping the mass loading of Ni strictly constant at 5 μg cm^{-2}. Remarkably, the presence of Fe suppressed the potential-induced coloration of the Ni almost entirely in the $Ni_{45}Fe_{55}$ catalyst; merely a weak residual potential-induced absorption remained visible reflecting the small percentage of Ni centers still undergoing redox processes (Figure 6a,b).

Changes in the position of the absorption maximum upon applied potential (1.5 V_{RHE}) were not observed as an effect of Fe incorporation. Due to the broad nature of the band and the weak absorption in the Ni−Fe centers, possible effects may have been masked. The wavelength dependent molar extinction coefficient was calculated on the basis of the total metal loading of Ni on the electrodes determined by elemental TXRF analysis (shown in Figure 6a, right axis), according to the following formula

$$\varepsilon(\lambda) = \frac{A(\lambda)}{c_{Ni} \cdot 10^3} \quad (6)$$

DOI: 10.1021/jacs.6b12250
J. Am. Chem. Soc. 2017, 139, 2070−2082

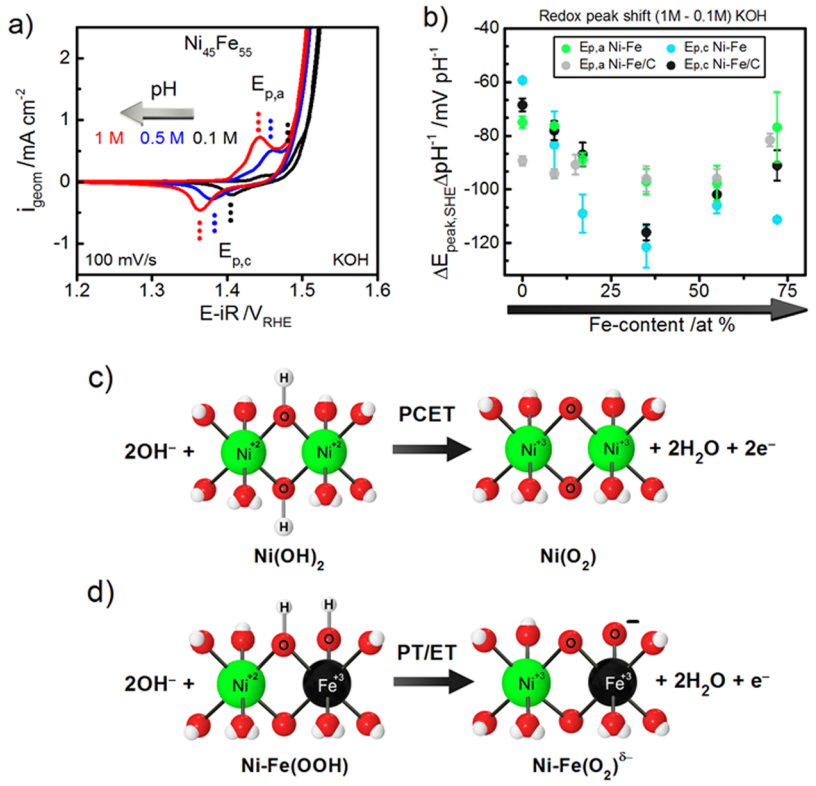

Figure 7. (a) CVs of the $Ni_{45}Fe_{55}$ catalyst in different electrolyte pHs, 0.1 M KOH (black), 0.5 M KOH (blue), and 1 M KOH (red), measured at 100 mV/s at 1600 rpm. The respective anodic and cathodic peak positions ($E_{p,c}$ and $E_{p,a}$) are indicated with dotted lines to guide the eye. (b) Peak shift of the Ni redox peak per pH unit ($\Delta E_{peak}/\Delta pH$) reported on the SHE scale of unsupported Ni−Fe and supported Ni−Fe/C catalysts as a function of Fe content. The catalyst composition is indicated as at. % Fe, determined by ICP-OES. (c) Schematic depiction of concerted coupled two-proton two-electron transfer (PCET) during the Ni oxidation step. (d) Two-proton transfer one-electron transfer (PT/ET) during deprotonation of mixed Ni−Fe(OOH), leading to oxidized Ni and accumulation of negative charge on the oxygen connected to the Fe site. Note that a formal charge balance in schemes c) and d) is reached, when assigning a positive charge to protonated bridging oxygens.

where $\varepsilon(\lambda)$ is the molar extinction coefficient in units L mol^{-1} cm^{-1}, $A(\lambda)$ is the wavelength dependent absorption, and c_{Ni} is the molar concentration of Ni on the electrode (mol cm^{-2}).

The extinction coefficient was estimated to increase up to 6500 and only to 200 L mol^{-1} cm^{-1} for Ni(OOH) and $Ni_{45}Fe_{55}$(OOH), respectively, at a potential of 1.5 V_{RHE}. Since the total metal loading of Ni was kept at a constant value for both the Ni and the Ni−Fe catalyst, the study confirms that Fe strongly suppresses the induced charged transfer of $Ni^{+2} \rightarrow Ni^{+3/+4}$, observed as a reduced absorption intensity at applied catalytic potential.

Our observations build on a previous report that demonstrated potential-induced coloration of solution-cast NiOOH and Ni−FeOOH catalyst thin films.[17] However, a quantitative analysis of the amount of oxidized Ni at catalytic OER potentials has previously not been established and we hereby show for the first time that Fe modifies the visible light absorption related to the oxidation of $Ni^{+2} \rightarrow Ni^{+3/+4}$ in a quantitative way. Our observations are in perfect agreement with a larger fraction of reduced Ni^{+2} centers in mixed Ni−Fe catalysts during catalytic potential, confirming findings in a previous XAS study from our group about low-valent Ni^{+2} in mixed Ni−Fe catalysts.[28] Potential cycling revealed that the absorption band of the Ni catalyst was rising right after the onset of the $Ni(OH)_2 \rightarrow$ NiOOH redox wave, and finished before OER commences. On the contrary, in the $Ni_{45}Fe_{55}$ catalyst, the UV−vis absorption started at slightly more anodic potentials, slightly overlapping with the OER catalytic process (Figure 6b). This concludes that Fe is suppressing the oxidation of Ni centers, shifting the onset of its oxidation closer to the OER onset potential and at pH 13 even into the catalytic potential range (see discussion below). Our data however do not allow unambiguous discrimination of whether the two competing oxidation processes (Ni oxidation and OER) are independent of each other.[28] Our results clearly demonstrate that Fe shifts the Ni oxidation anodically, and provides spectroscopic evidence to what appears as an OER catalytic process proceeding at low-valent Ni^{+2} centers in mixed Ni−Fe catalysts.

To further investigate the effect of the electrolyte pH on the UV−vis absorption band in the $Ni_{45}Fe_{55}$ catalyst, we applied a similar pH protocol during *operando* UV−vis measurements as previously in our DEMS study, gradually increasing the electrolyte concentration from 0.1 M → 0.5 M → 1 M KOH. Starting in the lowest electrolyte concentration of 0.1 M KOH (pH 13), the CVs revealed a small redox peak feature, confirmed by the weak potential-induced absorption at λ_{450nm} (Figure 6c). After a stable CV had been reached in 0.1 M KOH, the electrolyte was switched to 0.5 M KOH (pH 13.7). The Ni redox peak immediately shifted cathodically and grew in intensity. This was reflected in the UV−vis absorption band, which immediately responded to the increased electrolyte pH by an increased intensity along with an earlier onset potential for the oxidation (Figure 6d). After a stable CV had been reached in 0.5 M KOH, the electrolyte was switched to 1 M KOH (pH 13.9). The redox peak again shifted to more

DOI: 10.1021/jacs.6b12250
J. Am. Chem. Soc. 2017, 139, 2070−2082

cathodic potentials, and the absorption band intensified (Figure 6e). The response from the visible λ_{450nm} band was again consistent with a stronger coloration of the catalyst film in 1 M KOH, which suggests that a larger portion of oxidized $Ni^{+3/+4}$ centers were present in higher electrolyte pH. This is consistent with the decreased faradaic efficiency observed in the DEMS measurements at higher electrolyte pH. We noticed that, at the first CV cycle, there was a stronger absorption change than on all consecutive cycles (Figures 6a–e and S11a–c). This could confirm the presence of trapped oxidized Ni in the catalytic film, as discussed by Batchellor et al.,[3] or suggest Ni atoms in an average higher oxidation state. The coloration of the oxidized Ni centers was possible to remove by application of a slightly reducing potential, which returned the absorption to the initial level.

Our UV–vis measurements demonstrate that the reduction of oxidized $Ni^{+3/+4}$ centers is more difficult than the oxidation of Ni^{+2} centers, which might explain the "tail" observed in the DEMS measurements on the cathodic scan, assuming that the reduced centers relax through O_2 release. Both CVs and quasi-stationary-state measurements (Figure S12) confirmed that the oxidation commences more anodic in 0.1 M KOH compared to 0.5 and 1 M KOH. Notably, prior to the main oxidation wave in the $Ni_{45}Fe_{55}$ catalyst, we noticed spectral changes that could correspond to early formation of an oxidized species (preoxidation) starting before the onset of the Ni redox peak (Figure S11d). This was especially pronounced in 0.1 M KOH; however, it was also visible in 0.5 and 1 M KOH. The band was slightly more pronounced at higher wavelengths. In a recent ambient pressure XPS study by Ali-Löytty et. al, signals from an unknown oxide species, possibly a negatively charged "active oxygen species", were also detected at precatalytic potentials before the onset of the main Ni redox peak.[47]

Finally, to exclude that compositional changes accounted for the increased metal redox activity at high electrolyte pH, we estimated the amount of Ni and Fe on the electrodes after exposure to each respective electrolyte pH (0.1, 0.5, and 1 M KOH); see Figure S13. The samples were conditioned with an equivalent measurements protocol as in the UV–vis measurements, using identical conditions. The metal loadings were determined by TXRF analysis by dissolving the catalyst left on the electrode in acid. These measurements concluded that a fraction of Fe was lost upon exposure to KOH, and a small further loss due to increased electrolyte pH. However, the compositional changes were neglectible, and could not account for the increased metal redox activity.

In summary, our *operando* UV–vis studies enabled a quantitative estimation of the metal redox states in Ni–Fe oxide catalyst films during oxygen evolution conditions, even inside the OER range; they confirm the Fe-induced suppression of characteristic Ni-based spectral absorption of the film during scans into the catalytic OER potential range.

3.5. Non-Nernstian pH Effects and Decoupled Proton–Electron Transfer. A detailed analysis of the pH dependence of the characteristic catalyst Ni redox peak potentials revealed a surprising, previously overlooked *composition-sensitive* and *pH-sensitive* shift of both the anodic and the cathodic peak potentials (Figure 7a,b and Figure S14). Figure 7b shows the dependence of the Pourbaix slope ($\Delta E_{peak,SHE}/\Delta pH$) dependence on the Fe content of the catalysts. The pH-induced shifts of the peak potentials were near-Nernstian (~ −59 mV/pH) for the supported and unsupported NiOOH catalysts (0 at. % Fe) in unpurified as well as purified, rigorously Fe-free electrolytes. The ($\Delta E_{peak,SHE}/\Delta pH$) values observed for the Ni-only catalyst are in excellent agreement with similar Nernstian slopes of earlier studies.[35] However, at increasing Fe contents, the Pourbaix slopes ($\Delta E_{peak,SHE}/\Delta pH$) reached values as low as −120 mV/pH, peaking at around 37 at. % Fe. This constitutes a large deviation from the ideal Nernstian thermodynamics. The anodic scan exhibited a less pronounced shift than the cathodic scan; however, this is explained by the fact that the redox peak is hidden in the OER current, as revealed by the UV–vis spectro-electrochemical measurements in a previous section.

The −60 mV/pH Nernstian potential shift of Ni-only catalysts in Figure 7b can be explained in a straightforward manner by an *n*-proton coupled *n*-electron transfer[48,49] (PECT) schematically illustrated in Figure 7c ($n = 2$) according to

$$Ni^{+2}Ni^{+2}(OH)(OH) + 2OH^- \rightarrow Ni^{+3}Ni^{+3}(O)(O) + 2H_2O + 2e^- \quad (PCET) \tag{7}$$

We note that, to account for a thermodynamic Nernstian shift of −60 mV/pH, the proton/electron transfer in eq 7 does not necessarily have to proceed in a fully concerted manner.[33]

In contrast to the Nernstian behavior of Ni-only catalysts, the unusual super-Nernstian −120 mV/pH behavior in Figure 7b of the Ni–Fe catalysts is consistent with a two proton–one electron transfer[48,49] illustrated in Figure 7d according to

$$Ni^{+2}Fe^{+3}(OH)(OH) + 2OH^- \rightarrow Ni^{+3}Fe^{+3}(O)(O)^{\delta-} + 2H_2O + e^- \quad (PT/ET) \tag{8}$$

Schemes such as eq 8 would generate negatively charged oxygen ligands, which have been thought to be instrumental for the evolution of molecular oxygen, as such ligands react with neighboring vicinal/geminal OH ligands (lattice oxygens) or solvated OH^- forming so-called "active oxygen" species such as peroxide ("–O–OH" or "–O–O^-") and superoxide ("–O–O") ligands.[34,35,50] The thermodynamics do not allow any conclusions as to a concerted or serial nature of the two proton–one electron transfer. However, due to the experimental pH dependence of the catalytic OER rate at more anodic electrode potentials, a decoupled proton transfer appears conceivable. We propose that the initial proton abstraction from a terminal or bridged OH at a Fe^{+3} center is slow and results in the generation of a reactive $Ni^{+2}Fe^{+3}(OH)(O)^{\delta-}$ intermediate, followed by a fast subsequent concerted transfer of an electron and another proton, this time from a OH group attached to a redox active Ni^{+2} center. If the proton abstraction from Fe exhibits kinetic barriers, this would increase the required overpotential for proton abstraction with increasing Fe content. It would also diminish the experimentally observable population of the $Ni^{+2}Fe^{+3}(O)(O)^{\delta-}$ intermediate at a given overpotential.

Our data do not allow an unambiguous assignment at which metal center the negative charge is ultimately formed, nor if the negative charge is linked to a bridging oxygen or a terminal oxygen ligand. However, the anodic shift of the redox peak combined with the lack of evidence for any oxidized Fe^{+4},[28] suggest that the negatively charged oxygenate is more likely formed at a Fe. This would explain the delayed Ni oxidation and establish Fe as the catalytic active center. In fact, according to a recent isotope study involving 18-O exchange in CoO_x

DOI: 10.1021/jacs.6b12250
J. Am. Chem. Soc. 2017, 139, 2070–2082

catalyst by Koroidov et al., the O_2 is most probably formed by coupling of terminal intramolecular lattice oxygens.[51]

In summary, we report previously overlooked substantial non-Nernstian pH effects for unsupported and supported NiFe oxyhydroxide catalysts. We propose a two proton−one electron transfer scheme with a negatively charged species generated at the Fe center. This hypothesis is able to plausibly explain the experimental pH shifts of the voltammetric redox couple as well as the pH dependence of the OER activity. In addition, our hypothesis accounts for the anodic peak potential shifts with increasing Fe content and their diminished integral charge.

3.6. Local Atomic Structure under Catalytic OER Conditions. The local atomic structure and the metal redox states during oxygen evolution conditions were examined using *in situ* X-ray absorption spectroscopy (XAS), at the Ni and Fe *K*-edges. The catalysts were freeze-quenched at 1.63 V_{RHE} using liquid nitrogen after 30 min of chronoamperometric preconditioning at the given potential according to a reported method.[28,37,38] Catalysts were measured in 0.1 or 1 M KOH, where catalysts measured in 1 M KOH had not been exposed to 0.1 M KOH. The catalysts were kept under liquid nitrogen or liquid helium during transfer and throughout the measurements.

The Ni *K*-edge positions, shown in Figure 8a, were consistent with Ni absorbers in the carbon supported Ni catalyst (Ni/C) predominantly in an oxidation state of +3/+4 (or more precisely +3.7). This is in agreement with investigations of the unsupported Ni catalyst in an earlier study from our group.[28] The carbon supported $Ni_{45}Fe_{55}$/C catalyst investigated in 0.1 M KOH, in contrast to the unsupported $Ni_{45}Fe_{55}$ catalyst, showed a potential-induced Ni *K*-edge shift, however less pronounced in comparison to the Ni/C catalyst. Quantification of the oxidation states revealed a mixture of Ni^{+2} and $Ni^{+3/+4}$ atoms in the mixed $Ni_{45}Fe_{55}$/C catalyst and mainly Ni^{+2} centers in the $Ni_{45}Fe_{55}$ (fit parameters are listed in Table S2). This supports recent work from our group of unsupported Ni−Fe catalysts, showing that Fe results in a higher fraction of low-valent Ni^{+2}.[28] This also confirms that the carbon support increases the detectable amount of oxidized $Ni^{+3/+4}$ species compared to the unsupported Ni−Fe catalysts, which corroborates findings using DEMS, compatible with a larger redox peak in the Ni−Fe/C catalysts.

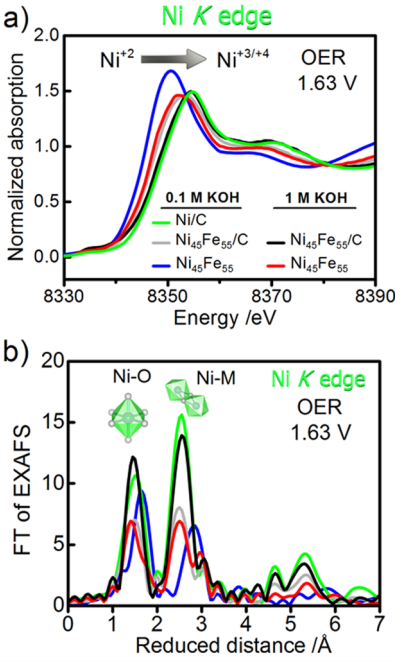

Figure 8. X-ray absorption spectroscopy (XAS) of unsupported and carbon supported Ni−Fe/C catalysts under a catalytic potential of 1.63 V_{RHE}, measured in 0.1 and 1 M KOH. (a) Ni K-edge XANES and (b) Ni K-edge FT-EXAFS for the catalysts shown in part a. Catalysts were freeze quenched after conditioning at the given potential for 30 min in 0.1 M KOH or 1 M KOH. Catalysts conditioned in 1 M KOH were not exposed to 0.1 M KOH prior to the measurements. Supporting measurements at the Fe K-edges are shown in Supporting Information Figure S15 and extended X-ray absorption fine structures in Figure S16. Fit parameters are listed in Tables S2 and S3. The catalyst composition is given as at. %. The legend in part a also applies to part b.

To investigate the effect of electrolyte pH, XANES was measured in 1 M KOH. These samples had not been exposed to 0.1 M KOH in order to rule out possible effects from pre-exposure to 0.1 M KOH. The Ni *K*-edge showed a stronger potential-induced shift which could be fitted with a larger fraction of oxidized $Ni^{+3/+4}$ species present in both the unsupported $Ni_{45}Fe_{55}$ and the supported $Ni_{45}Fe_{55}$/C catalysts in 1 M KOH (Figure 8a and fit parameters in Table S2). This is consistent with the findings using both DEMS and UV−vis spectroelectrochemistry that higher electrolyte pH facilitates the metal oxidation process, seen as an enhanced redox peak feature.

The Fe *K*-edge did not undergo an observable shift under catalytic potential, and Fe was consistently in oxidation state +3 (see Figure S15a and fit parameters in Table S3). This is in accordance with earlier findings from our group of the unsupported catalysts[28] and in agreement with work from Friebel et al.[24] While there exists a single report on the formation of Fe^{+4} under catalytic potential,[30] all other reports arrived at the conclusion that the overwhelming fraction of Fe centers in Ni−Fe/C catalysts does indeed remain in oxidation state +3. According to a recent DFT+U study, different analogous NiOOH structures may favor different local atomic environments also with respect to oxidation state.[29]

The Fourier-transformed extended X-ray absorption fine structure (FT-EXAFS) of the Ni/C catalyst (Figure 8b) revealed explicit octahedral coordination of Ni−O at a distance of 1.88 Å and Ni−M of 2.82 Å, the latter ascribed to di-μ-oxo-bridged metal (see insets in Figure 8b for motifs). The short coordination distances under a catalytic potential were consistent with a γ-NiOOH phase.[24,28,52,53] The $Ni_{45}Fe_{55}$ and $Ni_{45}Fe_{55}$/C catalysts in 1 M KOH showed split Ni−O and Ni−M coordination distances, which impart the presence of partly reduced Ni^{+2} and partly oxidized $Ni^{+3/+4}$ atoms. This is also evident from the suppressed *K*-edge shift of the mixed Ni−Fe catalysts in comparison to the Ni/C catalyst. The fraction of reduced Ni^{+2} centers (long distance) could be well represented by Ni−O shells coordinated at 2.04 Å and Ni−M shells at 3.08 Å, consistent with a α-$Ni(OH)_2$ phase.[24,28] The absence of a potential-induced Fe *K*-edge shift and a lack of contraction of the Ni−O bond supports the absence of a metal oxidation state change of Fe (Figure S15b). Nevertheless, a contraction in the Fe−M coordination appeared as a response to the oxidized fraction of $Ni^{+3/+4}$ centers, with an additional coordination distance arising at 2.93 Å, supporting that Fe was incorporated to form well-mixed Ni−Fe centers. X-ray absorption fine structure is shown in Supporting Information Figure S16, and complete fit parameters are listed in Tables S2 and S3.

DOI: 10.1021/jacs.6b12250
J. Am. Chem. Soc. 2017, 139, 2070−2082

We conclude that the carbon supported Ni−Fe/C catalysts exhibited a generally larger fraction of oxidized Ni^{+4} centers in comparison to the unsupported catalysts,[28] presumably due to the enhanced electrolyte accessibility to more catalytic centers. Increased electrolyte OH^- concentration also increased the detectable amounts of oxidized $Ni^{+3/+4}$ centers showing that higher pH facilitates the metal oxidation step. On the other hand, the fraction of oxidized $Ni^{+3/+4}$ in mixed Ni−Fe/C centers was consistently lower in comparison to the Ni/C catalyst, also confirming that Fe suppresses Ni oxidation.[27,28] The XAS investigations confirmed both findings using DEMS and UV−vis spectroelectrochemistry, where faradaic efficiency of O_2 and spectroscopic potential-induced coloration associated with charge transfer processes of the Ni metal were used as sensors to track catalyst redox state changes in mixed Ni−Fe catalysts.

4. CONCLUSIONS

We have presented a detailed study of the effects of high surface-area conductive supports and the electrolyte pH on the OER catalysis of Ni−Fe oxyhydroxide catalysts under alkaline conditions. New insights and important conclusions were obtained from a combination of voltammetric, *in situ* electrochemical UV−vis, *operando* electrochemical mass spectrometric (DEMS), and *in situ* cryo X-ray absorption spectroscopic data. In particular, we address the paradox of muted Ni redox activity with increasing Fe content.

Compared to the unsupported reference catalyst at pH 13, catalyst support and pH values >13 caused a substantial cathodic shift and enhancement of the voltammetric catalyst redox activity in the precatalytic potential range prior to the OER onset. *Operando* UV−vis data confirmed this finding, showing a more cathodic onset of generation of oxidized Ni species with increasing pH. Both support and electrolyte pH showed strongly enhancement effects on the catalytic OER activity, however, in distinctly different manners. Supported NiFe oxyhydroxide catalysts, with their higher particle dispersion, allow for a larger population of metal centers to be electrochemically addressable and accessible. This interpretation was consistent with lower DEMS-derived faradaic efficiencies for O_2 and slightly higher XANES/EXAFS-derived average Ni oxidation states of the supported catalysts. With or without support, UV−vis, DEMS, and XANES/EXAFS data all evidenced that Fe suppressed the Ni redox behavior relative to the Ni(OOH) catalyst.

Our study further revealed a dramatic effect of Fe^{+3} centers on the Ni redox peak potential shift with pH. Data revealed a gradual transition from an ideal Nernstian to a strongly non-Nernstian cathodic potential shift with increasing Fe; we rationalized this in terms of a transition from a two proton−two electron PCET process to a two proton−one electron (PT/ET) transfer, involving the generation of negatively charged oxygen ligands at the Fe centers. If the deprotonation of the Fe-bound OH is assumed slow but necessary for subsequent proton/electron redox transfers at adjacent Ni centers, this would provide a plausible explanation for the long-standing paradox of the anodic shifts of the Ni redox peaks with higher Fe content, despite earlier OER onset. Together, the refined mechanistic picture is able to consistently explain most major present and previous observations, a significant step forward in our understanding of the OER catalysis of this catalyst system.

■ ASSOCIATED CONTENT

Supporting Information

The Supporting Information is available free of charge on the ACS Publications website at DOI: 10.1021/jacs.6b12250.

Additional structural characterization and supporting electrochemical characterization (PDF)

■ AUTHOR INFORMATION

Corresponding Authors

*holger.dau@fu-berlin.de

*pstrasser@tu-berlin.de

ORCID

Peter Strasser: 0000-0002-3884-436X

Notes

The authors declare no competing financial interest.

■ ACKNOWLEDGMENTS

This project received financial support from the Bundesministerium für Bildung und Forschung (BMBF) under grant reference numbers 03SF0433A "MEOKATS" and 03SF0523A "CO2EKAT". S.D. acknowledges support by German Research Foundation (DFG) via grant STR 596/8-1 ("Reversible seawater electrolysis"). We thank the Helmholtz-Zentrum Berlin (HZB) for allocation of synchrotron radiation beamtime at KMC-1 and KMC-3 (BESSY synchrotron, Berlin Adlershof), and we gratefully acknowledge support by Marcel Mertin, Dr. Franz Schäfers, and Dr. Ivo Zizak (all BESSY/HZB). H.D. thanks UniCat for partial financial support.

■ REFERENCES

(1) Corrigan, D. A. *J. Electrochem. Soc.* **1987**, *134*, 377.

(2) Louie, M. W.; Bell, A. T. *J. Am. Chem. Soc.* **2013**, *135*, 12329.

(3) Batchellor, A. S.; Boettcher, S. W. *ACS Catal.* **2015**, *5*, 6680.

(4) Trotochaud, L.; Ranney, J. K.; Williams, K. N.; Boettcher, S. W. *J. Am. Chem. Soc.* **2012**, *134*, 17253.

(5) Smith, A. M.; Trotochaud, L.; Burke, M. S.; Boettcher, S. W. *Chem. Commun.* **2015**, *51*, 5261.

(6) McCrory, C. C. L.; Jung, S.; Ferrer, I. M.; Chatman, S. M.; Peters, J. C.; Jaramillo, T. F. *J. Am. Chem. Soc.* **2015**, *137*, 4347.

(7) Oliver-Tolentino, M. A.; Vázquez-Samperio, J.; Manzo-Robledo, A.; González-Huerta, R. d. G.; Flores-Moreno, J. L.; Ramírez-Rosales, D.; Guzmán-Vargas, A. *J. Phys. Chem. C* **2014**, *118*, 22432.

(8) Landon, J.; Demeter, E.; Inoglu, N.; Keturakis, C.; Wachs, I. E.; Vasic, R.; Frenkel, A. I.; Kitchin, J. R. *ACS Catal.* **2012**, *2*, 1793.

(9) Fominykh, K.; Chernev, P.; Zaharieva, I.; Sicklinger, J.; Stefanic, G.; Döblinger, M.; Müller, A.; Pokharel, A.; Böcklein, S.; Scheu, C.; Bein, T.; Fattakhova-Rohlfing, D. *ACS Nano* **2015**, *9*, 5180.

(10) Gong, M.; Li, Y.; Wang, H.; Liang, Y.; Wu, J. Z.; Zhou, J.; Wang, J.; Regier, T.; Wei, F.; Dai, H. *J. Am. Chem. Soc.* **2013**, *135*, 8452.

(11) Qiu, Y.; Xin, L.; Li, W. *Langmuir* **2014**, *30*, 7893.

(12) Görlin, M.; Gliech, M.; Ferreira de Araújo, J.; Dresp, S.; Bergmann, A.; Strasser, P. *Catal. Today* **2016**, *262*, 65.

(13) Dionigi, F.; Strasser, P. *Adv. Energy Mater.* **2016**, *6*, 1614.

(14) Dresp, S.; Luo, F.; Schmack, R.; Kuhl, S.; Gliech, M.; Strasser, P. *Energy Environ. Sci.* **2016**, *9*, 2020.

(15) Luo, J.; Im, J.-H.; Mayer, M. T.; Schreier, M.; Nazeeruddin, M. K.; Park, N.-G.; Tilley, S. D.; Fan, H. J.; Grätzel, M. *Science* **2014**, *345*, 1593.

(16) Wang, L.; Dionigi, F.; Nguyen, N. T.; Kirchgeorg, R.; Gliech, M.; Grigorescu, S.; Strasser, P.; Schmuki, P. *Chem. Mater.* **2015**, *27*, 2360.

(17) Trotochaud, L.; Mills, T. J.; Boettcher, S. W. *J. Phys. Chem. Lett.* **2013**, *4*, 931.

DOI: 10.1021/jacs.6b12250
J. Am. Chem. Soc. 2017, 139, 2070−2082

(18) Morales-Guio, C. G.; Mayer, M. T.; Yella, A.; Tilley, S. D.; Grätzel, M.; Hu, X. *J. Am. Chem. Soc.* **2015**, *137*, 9927.
(19) Trotochaud, L.; Young, S. L.; Ranney, J. K.; Boettcher, S. W. *J. Am. Chem. Soc.* **2014**, *136*, 6744.
(20) Godwin, I. J.; Lyons, M. E. G. *Electrochem. Commun.* **2013**, *32*, 39.
(21) Yu, X.; Zhang, M.; Yuan, W.; Shi, G. *J. Mater. Chem. A* **2015**, *3*, 6921.
(22) Lu, X.; Zhao, C. *Nat. Commun.* **2015**, *6*, 1.
(23) Ma, W.; Ma, R.; Wang, C.; Liang, J.; Liu, X.; Zhou, K.; Sasaki, T. *ACS Nano* **2015**, *9*, 1977.
(24) Friebel, D.; Louie, M. W.; Bajdich, M.; Sanwald, K. E.; Cai, Y.; Wise, A. M.; Cheng, M.-J.; Sokaras, D.; Weng, T.-C.; Alonso-Mori, R.; Davis, R. C.; Bargar, J. R.; Nørskov, J. K.; Nilsson, A.; Bell, A. T. *J. Am. Chem. Soc.* **2015**, *137*, 1305.
(25) Bode, H.; Dehmelt, K.; Witte, J. *Electrochim. Acta* **1966**, *11*, 1079.
(26) Corrigan, D. A.; Knight, S. L. *J. Electrochem. Soc.* **1989**, *136*, 613.
(27) Bates, M. K.; Jia, Q.; Doan, H.; Liang, W.; Mukerjee, S. *ACS Catal.* **2016**, *6*, 155.
(28) Görlin, M.; Chernev, P.; Ferreira de Araújo, J.; Reier, T.; Dresp, S.; Paul, B.; Krähnert, R.; Dau, H.; Strasser, P. *J. Am. Chem. Soc.* **2016**, *138*, 5603.
(29) Conesa, J. C. *J. Phys. Chem. C* **2016**, *120*, 18999.
(30) Chen, J. Y. C.; Dang, L.; Liang, H.; Bi, W.; Gerken, J. B.; Jin, S.; Alp, E. E.; Stahl, S. S. *J. Am. Chem. Soc.* **2015**, *137*, 15090.
(31) Browne, M. P.; Stafford, S.; O'Brien, M.; Nolan, H.; Berner, N. C.; Duesberg, G. S.; Colavita, P. E.; Lyons, M. E. G. *J. Mater. Chem. A* **2016**, *4*, 11397.
(32) Enman, L. J.; Burke, M. S.; Batchellor, A. S.; Boettcher, S. W. *ACS Catal.* **2016**, *6*, 2416.
(33) Koper, M. T. M. *Phys. Chem. Chem. Phys.* **2013**, *15*, 1399.
(34) Trześniewski, B. J.; Diaz-Morales, O.; Vermaas, D. A.; Longo, A.; Bras, W.; Koper, M. T. M.; Smith, W. A. *J. Am. Chem. Soc.* **2015**, *137*, 15112.
(35) Diaz-Morales, O.; Ferrus-Suspedra, D.; Koper, M. T. M. *Chemical Science* **2016**, *7*, 2639.
(36) Jusys, Z.; Massong, H.; Baltruschat, H. *J. Electrochem. Soc.* **1999**, *146*, 1093.
(37) Risch, M.; Ringleb, F.; Kohlhoff, M.; Bogdanoff, P.; Chernev, P.; Zaharieva, I.; Dau, H. *Energy Environ. Sci.* **2015**, *8*, 661.
(38) Bergmann, A.; Martinez-Moreno, E.; Teschner, D.; Chernev, P.; Gliech, M.; de Araujo, J. F.; Reier, T.; Dau, H.; Strasser, P. *Nat. Commun.* **2015**, *6*, 1.
(39) Ankudinov, A. L.; Ravel, B.; Rehr, J. J.; Conradson, S. D. *Phys. Rev. B: Condens. Matter Mater. Phys.* **1998**, *58*, 7565.
(40) Rehr, J. J.; Albers, R. C. *Rev. Mod. Phys.* **2000**, *72*, 621.
(41) Maca, T.; Vondrák, J.; Sedlaříková, M. *ECS Trans.* **2011**, *40*, 119.
(42) Hall, D. S.; Lockwood, D. J.; Bock, C.; MacDougall, B. R. *Proc. R. Soc. London, Ser. A* **2015**, *471*, 20140792.
(43) Stern, L.-A.; Hu, X. *Faraday Discuss.* **2014**, *176*, 363.
(44) Burke, M. S.; Kast, M. G.; Trotochaud, L.; Smith, A. M.; Boettcher, S. W. *J. Am. Chem. Soc.* **2015**, *137*, 3638.
(45) Jusys, Z.; Kaiser, J.; Behm, R. J. *Electrochim. Acta* **2004**, *49*, 1297.
(46) Oh, H.-S.; Nong, H. N.; Reier, T.; Bergmann, A.; Gliech, M.; Ferreira de Araújo, J.; Willinger, E.; Schlögl, R.; Teschner, D.; Strasser, P. *J. Am. Chem. Soc.* **2016**, *138*, 12552.
(47) Ali-Löytty, H.; Louie, M. W.; Singh, M. R.; Li, L.; Sanchez Casalongue, H. G.; Ogasawara, H.; Crumlin, E. J.; Liu, Z.; Bell, A. T.; Nilsson, A.; Friebel, D. *J. Phys. Chem. C* **2016**, *120*, 2247.
(48) Bockris, J. O. M.; Reddy, A. K. N.; Gamboa-Aldeco, M. *Modern Electrochemistry 2A: Fundamentals of Electrodics*, 2nd ed.; Plenum US: New York, 1998; Vol. 2A.
(49) Hamann, C. H.; Hamnett, A.; Vielstich, W. *Electrochemistry*, 2nd ed.; Wiley: Weinheim, Germany, 2007.
(50) Zhang, M.; de Respinis, M.; Frei, H. *Nat. Chem.* **2014**, *6*, 362.
(51) Koroidov, S.; Anderlund, M. F.; Styring, S.; Thapper, A.; Messinger, J. *Energy Environ. Sci.* **2015**, *8*, 2492.
(52) O'Grady, W. E.; Pandya, K. I.; Swider, K. E.; Corrigan, D. A. *J. Electrochem. Soc.* **1996**, *143*, 1613.
(53) Risch, M.; Klingan, K.; Heidkamp, J.; Ehrenberg, D.; Chernev, P.; Zaharieva, I.; Dau, H. *Chem. Commun.* **2011**, *47*, 11912.

DOI: 10.1021/jacs.6b12250
J. Am. Chem. Soc. 2017, 139, 2070−2082